IVYSPRING
INTERNATIONAL PUBLISHER

Theranostics

2019; 9(2): 369-380. doi: 10.7150/thno.29817

Research Paper

Fabrication of Red Blood Cell-Based Multimodal Theranostic Probes for Second Near-Infrared Window Fluorescence Imaging-Guided Tumor Surgery and Photodynamic Therapy

Peiyuan Wang[1,2,3], Xuandong Wang[1,2,3], Qiang Luo[1,2,3], Yang Li[1,2,3], Xiaoxiao Lin[1,2,3], Lingling Fan[4], Yun Zhang[1,2,3], Jingfeng Liu[1,2,3]✉, Xiaolong Liu[1,2,3]✉

1. Key Laboratory of Design and Assembly of Functional Nanostructures, Fujian Institute of Research on the Structure of Matter, Chinese Academy of Sciences, Fuzhou 350002, P. R. China.
2. The United Innovation of Mengchao Hepatobiliary Technology Key Laboratory of Fujian Province, Mengchao Hepatobiliary Hospital of Fujian Medical University, Fuzhou 350025, P. R. China.
3. Department of Translational Medicine, Xiamen Institute of Rare Earth Materials, Chinese Academy of Sciences, Xiamen 361024, P. R. China.
4. Obstetrics and Gynecology Hospital, Fudan University, Shanghai 200011, P. R. China.

✉ Corresponding authors: X. Liu. E-mail: xiaoloong.liu@gmail.com and J. Liu. E-mail: drjingfeng@126.com

Received: 2018.09.10; Accepted: 2018.12.06; Published: 2019.01.01

Abstract

The therapeutic efficacy of fluorescence image-guided tumor surgery and photodynamic therapy (PDT) is impaired by the penetration depth limitation, low signal-to-noise ratio of traditional first near-infrared window (NIR I) fluorescence and the hypoxic tumor microenvironment. Here, a "red blood cell-based multimodal probe" was proposed to achieve enhanced tumor targeting and retention of fluorescent probes after an intravenous injection, so that second near-infrared window (NIR II) fluorescence bioimaging-guided complete tumor resection and high-efficiency photodynamic therapy could then be realized.

Methods: The hexanoic acid ester-modified rose bengal (RB-HA), RGD (Arginine-Glycine-Aspartic) peptide and avidin were covalently coupled onto amine-modified upconversion nanoparticles (UCNPs) *via* EDC/NHS reaction (UCNPs@RB@RGD@avidin). Afterwards, the complex of ICG with bovine serum albumin (BSA) was loaded into RBCs through hypotonic dialysis (RBC@ICG). Then, the membrane proteins of RBC@ICG were biotinylated by biotin-modified phospholipids (RBC@ICG@biotin). Finally, the RBCp (Red Blood Cell based probe) was obtained by crosslinking UCNPs@RB@RGD@avidin to RBC@ICG@biotin through the interaction of avidin and biotin. The obtained multimodal RBCp was extensively characterized, both *in vitro* and *in vivo*, including analysis of chemical, physical and fluorescent features, O_2 delivery ability, tumor accumulation, NIR II fluorescence bioimaging ability, photodynamic therapeutic efficiency, and biosafety.

Results: The RBCp experienced efficient tumor targeting and long tumor retention for almost 4 h after intravenous injection, and the superior signal-to-noise ratio at the optimal time window can be used for guiding precise tumor resection under an 808-nm laser irradiation to facilitate lymph popliteal metastasis surgical delineation. Meanwhile, the RBCp can provide laser-responsive O_2 release to enhance the PDT efficiency of popliteal lymph node metastasis under NIR II fluorescence bioimaging guidance. These excellent performances obviously lead to remarkably enhanced synergistic therapeutic effects of tumor surgery and metastatic inhibition.

Conclusion: The proposed strategy will develop a new platform to increase surgical resection completeness and improve PDT efficiency, resulting in the successful and complete inhibition of tumor and metastasis, which could offer a promising approach for the clinical translation of malignant tumor treatment.

Key words: second near-infrared window fluorescence, indocyanine green, tumor surgery, oxygen delivery, photodynamic therapy

Introduction

For most liver malignancies, the ideal first-line treatment is complete surgical resection. Intraoperative imaging is the most favorable method that is capable of a precise visualization of tumor margins and observation of other ultra-small metastases [1-5]. Fluorescence imaging offers the promise of safe, noninvasive detection along with other advantages, including ultrahigh resolution, real-time observation, and superior specificity for ultra-small tumors during diagnostic and intraoperative surgical procedures [6-9]. Compared with visible wavelengths (400 - 650 nm), the fluorescence imaging capabilities of the first near-infrared window (NIR I, 650 - 900 nm) conventional contrast agents, such as the FDA-approved indocyanine green (ICG) and methylene blue (MB), have been demonstrated to be far superior [10]. However, these contrast agents are usually limited by shallow tissue penetration (~1 mm) and low signal-to-noise ratio resulting from photon tissue scattering and tissue autofluorescence [11-13]. Owing to the reduced photon scattering, deeper tissue penetration (~10 mm), and lower autofluorescence, contrast agents in the second near-infrared window (NIR II, 1000 - 1700 nm) represent promising candidates for both preoperative imaging and intraoperative guidance; fluorescence imaging in this region is more favorable than that within the visible and traditional NIR I regions [14-20]. Therefore, the exploration of clinically approved NIR II probes may give rise to the next generation of *in vivo* fluorescence bioimaging contrast agents for tumor surgery guidance.

As another favorable noninvasive treatment for tumors, photodynamic therapy (PDT) can convert O_2 into massive concentrations of reactive oxygen species (ROS) in order to efficiently kill tumor cells upon laser irradiation [21-26]. Several studies have unequivocally demonstrated that the hypoxic tumor microenvironment has an obviously adverse effect on PDT efficiency [27-29]. Meanwhile, PDT itself could further strengthen the hypoxic condition after O_2 consumption following tumor vessel shutdown effects [30,31]. These facts emphasize the importance of O_2 supply in PDT and the significance of simultaneous codelivery of both O_2 and photosensitizers in this treatment [32-35]. Over the past years, numerous anti-hypoxia strategies have been developed to overcome tumor hypoxia, such as perfluorocarbon nanoparticles for O_2 and photosensitizer codelivery [36,37], hyaluronidase for oxygenation enhancement [38], and MnO_2 nanoparticles for oxygenation with cytoplasmic H_2O_2 catalysis [39-41]. However, these methods fail to match the sophistication of hindering innate biological entities [42]. To this point, there are no studies focused on the aforementioned directions of accomplishing codelivery of NIR II probes, O_2 and photosensitizers with specialized entities to realize NIR II fluorescence bioimaging-guided tumor surgery and controllable O_2 delivery to hypoxic tumors for PDT enhancement.

Commercially available NIR I dyes, such as the FDA-approved agent ICG, are also suitable for *in vivo* NIR II fluorescence imaging because the absorbance bands extend into the NIR II region beyond 1500 nm; this particular dye also exhibits a relatively higher quantum yield than some existing commercially available NIR II fluorophores [43,44], even though its emission peak is not centered in the NIR II region. Meanwhile, as the “innate transporters” in our blood circulatory system for O_2 delivery, red blood cells (RBCs) have long been studied for drug delivery [45,46]. Inspired by the aforementioned studies, in this work, we fabricated RBCp for NIR II fluorescence bioimaging-guided tumor surgery and light-triggered O_2 release to enhance PDT efficiency. The photosensitizer (rose bengal, RB) and the RGD peptide (for $\alpha_v\beta_3$-integrin targeting) functionalized UCNPs were installed onto the surface of ICG-loaded RBCs to fabricate RBCp. The herein reported RBCp exhibits the abilities of both efficient tumor targeting and tumor retention. Under an 808-nm laser irradiation, the intratumoral RBCp could absorb heat and swell, resulting in ICG burst and O_2 release. Then, the tumor can be successfully resected with the NIR II fluorescence bioimaging navigation. Furthermore, the PDT efficiency for metastatic tumors, which could be greatly enhanced because of the increased O_2 concentration inside tumors, can also be monitored by NIR II fluorescence bioimaging. Taken together, this novel RBC-based multimodal theranostic probe for tumor surgical resection and site-specific PDT of metastatic tumors under NIR II fluorescence bioimaging guidance might represent a promising approach for the efficient treatment of different malignant tumors.

Results and Discussion

RBCp fabrication

Figure 1 shows a schematic illustration of the RBCp fabrication. ROS can be produced through photosensitizers which can be activated by visible light generated from UCNPs, wherein the UCNPs play a vital role as an energy transducer under NIR light [48]. Here, as the 980-nm laser triggered component of the PDT platform, the lanthanide doped $NaGdF_4$:Yb,Er@$NaGdF_4$ nanocrystals with core-shell nanostructure were synthesized according to the previously reported successive layer-by-layer strategy with a quantum yield of 0.51±0.06 % (**Figure 1** and **Figure 2A-B**) [49]. These nanoprobes have uniform particle sizes of approximately 40 nm and a highly efficient 550 nm upconverting luminescence under 980 nm laser irradiation to trigger photosensitization for $^1O_2$ generation (**Figure 2E**). To facilitate biological applications, the hydrophobic UCNPs with an oleic acid capping were transferred to the hydrophilic phase after adding amine-phospholipids (DSPE-PEG$_{2000}$-NH$_2$) *via* van der Waals interactions [50]. The amine-phospholipid-modified UCNPs were very stable in both *in vitro* and *in vivo* conditions (**Figures S1-S2**). Then, the hexanoic acid ester-modified rose bengal (RB-HA), the RGD peptide as tumor targeting motif and avidin (specific biotin-binding protein) were covalently coupled onto amine-modified UCNPs *via* EDC/NHS reaction (UCNPs@RB@RGD@avidin) (**Figure 1**). Furthermore, the NIR II fluorescence signal of the clinically used NIR I probe ICG was investigated. Recording the emission spectra on a system sensitive to both NIR I and NIR II fluorescence, such as an InGaAs detector-based system (100 ms exposure time and 1000 nm long-pass filter), shows that ICG emission extends well into the NIR II region (**Figure 2F**). To obtain RBC-based multimodal theranostic probes, the RBCs were first obtained from healthy female nude mice. Second, the complexes of ICG with bovine serum albumin (BSA) were loaded into RBCs through the strategy of hypotonic dialysis (RBC@ICG) to avoid destructing the RBC membranes [47,51]. Third, to link the avidin-modified nanoprobes, the membrane proteins of RBC@ICG were biotinylated by biotin-modified phospholipids (DSPE-PEG$_{2000}$-biotin) (RBC@ICG@biotin) [47]. Finally, according to the bio-interaction of avidin and biotin, the UCNPs@RB@RGD@avidin were then crosslinked with RBC@ICG@biotin (**Figure 1**). The loading capacities of RGD, RB, and UCNPs on RBCs were evaluated, showing saturated RGD, RB, and UCNP loading ratios of approximately 12% (w/w), 27% (w/w), and 40% (w/w) at the fixed feeding concentrations of UCNPs, RGD and RB, respectively. Moreover, the absorbance of total hemoglobin (**Figure S3**), the change of dissolved O_2 concentration ($\triangle$ dissolved O_2, **Figure S4**) and zeta-potential of RBCs (**Figure S5**) were carefully studied during the stepwise functionalization process; the results showed that all of these key characteristic features were only minimally changed during the functionalization process, as compared with the natural unmodified RBCs, demonstrating little effects of the modification process on the O_2 carrying characteristics and surface charge. Moreover, the RBCp were also very stable both in PBS and serum buffer conditions (**Figure S6**). Furthermore, scanning electron microscope (SEM) and transmission electron microscope (TEM) images demonstrated that the UCNPs were successfully anchored onto the membranes of RBCs, which did not show any alteration of the cell morphology after modification so that the normal biconcave shape of RBCp was maintained (**Figure 2C-D** and **Figure S7**). Meanwhile, both the morphology and size of RBCs (~7 μm) were maintained after cross-linking the UCNPs@RB@RGD@avidin, further demonstrating that the total amount of O_2 in the RBCp had not leaked (**Figure 2C-D**). Before the *in vivo* application of RBCp, the cellular uptake of our RBCp was evaluated through CLSM imaging. As shown in **Figure S8**, our RBCp was efficiently taken up by HepG2 cells, demonstrating the effective tumor cell targeting ability of RGD modification. After a 24 h incubation, the cell counting kit-8 assay was then used to evaluate the relative cell viabilities. The results indicated that the HepG2 cells possessed more than 90% viability when incubated with 250 μg/mL RBCp, suggesting the low cytotoxicity of the RBC-based multimodal probes (**Figure S9**).

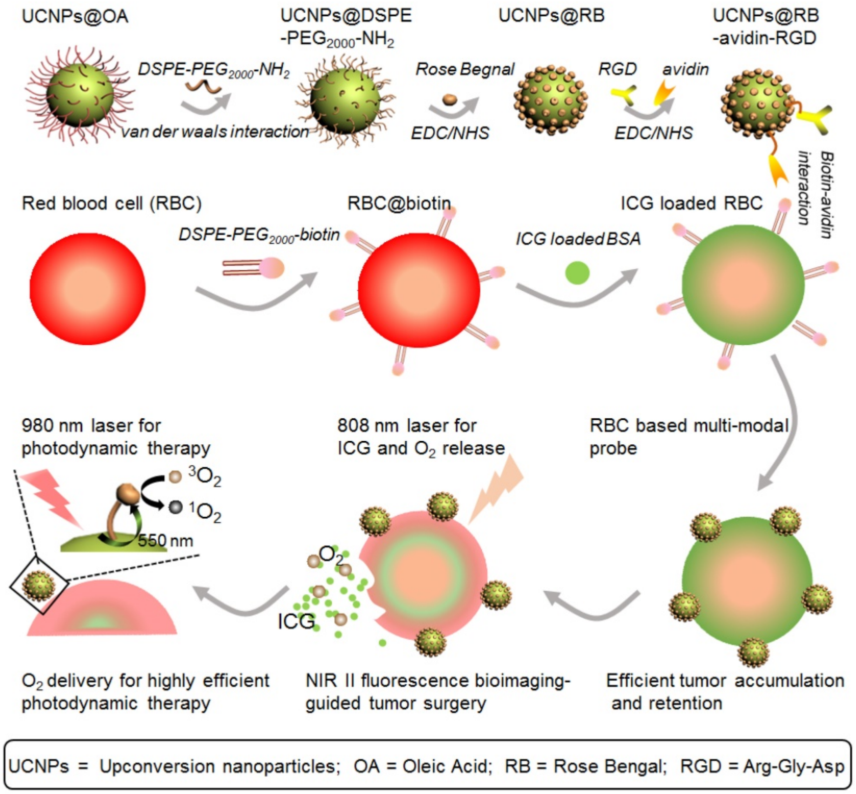

Figure 1. A schematic illustration of RBCp fabrication. With an 808-nm laser irradiation, RBCp can continuously release ICG and O_2, which can be applied for NIR II fluorescence bioimaging-guided tumor surgery as well as to enhance NIR II fluorescent bioimaging-guided photodynamic therapy.

ICG and O_2 release of RBCp

Inspired by the successful RBCp fabrication, we then carefully studied the properties of the fabricated RBCp. First, in order to estimate the advantages of the NIR II fluorescence of ICG, the penetration depths of both NIR I and NIR II fluorescence were studied. The results show that the penetration depth of fluorescence in NIR II (~8 mm) was almost two-fold higher than that of NIR I (~4 mm) (**Figure 3A**); the signal-to-noise ratio of ICG in the NIR II (~7.8) was also three-fold higher than that in the NIR I (~2.1) at 4 mm depth (**Figure 3B-C**), further indicating that the commercially available, FDA-approved NIR I dye ICG can be applied for in *vivo* NIR II fluorescence imaging. Afterwards, we examined whether the fabricated RBCp can realize site-specific O_2 release with a laser activation at 808 nm and 0.5 W/cm^2; therefore, the dissolved O_2 in aqueous solution was evaluated by a dissolved oxygen detector following the laser irradiation at 808 nm. As shown in **Figure 3D**, the △dissolved O_2 concentration of RBCp was continuously increased as a function of irradiation time. Conversely, only a trace amount of O_2 release was observed in the control group of RBCp without 808-nm laser irradiation, and almost no O_2 release was detected in response to 808-nm laser irradiation alone or from pure RBCs with 808-nm laser irradiation. This is mainly owing to the high temperature-induced oxygenated hemoglobin (HbO_2) release from RBCp as well as the high temperature-induced O_2 dissociation from the HbO_2. These *in vitro* dissolved O_2 results demonstrate that O_2 release from RBCp can be precisely activated by an 808-nm laser irradiation. Moreover, to directly observe O_2 generation in the cytoplasm, a confocal laser scanning microscope (CLSM) experiment was subsequently carried out. After RBCp incubation with HepG2 cells, the fluorescence signals of a commercially available O_2 dye, tris(4,7-diphenyl-1,10-phenanthroline)ruthenium (II) dichloride ($Ru(dpp)_3^{2+}$), were significantly quenched by an intracellular O_2 release after irradiation with an 808-nm laser (0.5 W/cm^2) for various minutes (0 ~ 10 min) (**Figure 3E**), further demonstrating that a significant amount of intracellular O_2 can be precisely activated and continuously released. Meanwhile, the RBCp structures were completely destroyed and O_2 release was most obvious with a laser exposure duration of 10 min (**Figure S10**). Moreover, we also observed that the ICG in a medium with serum was very stable upon an 808-nm laser irradiation, but that it was relatively unstable in PBS buffer upon laser irradiation, as demonstrated by its fluorescence intensity change (**Figure S11**). Meanwhile, ICG could also be readily released from the RBCp upon an 808-nm laser irradiation with similar kinetics as O_2 release (**Figure S12**). These results demonstrated that both ICG and O_2 could be successfully released after laser irradiation. Based on the aforementioned results, we also studied the intratumor O_2 release *via* photoacoustic (PA) imaging. The blood O_2 saturation in the HepG2 tumor vasculature was evaluated by measuring oxyhemoglobin. There is a significant oxyhemoglobin signal increase after an intravenous injection of RBCp in the tail vein under an 808-nm laser irradiation, resulting in the enhancement of

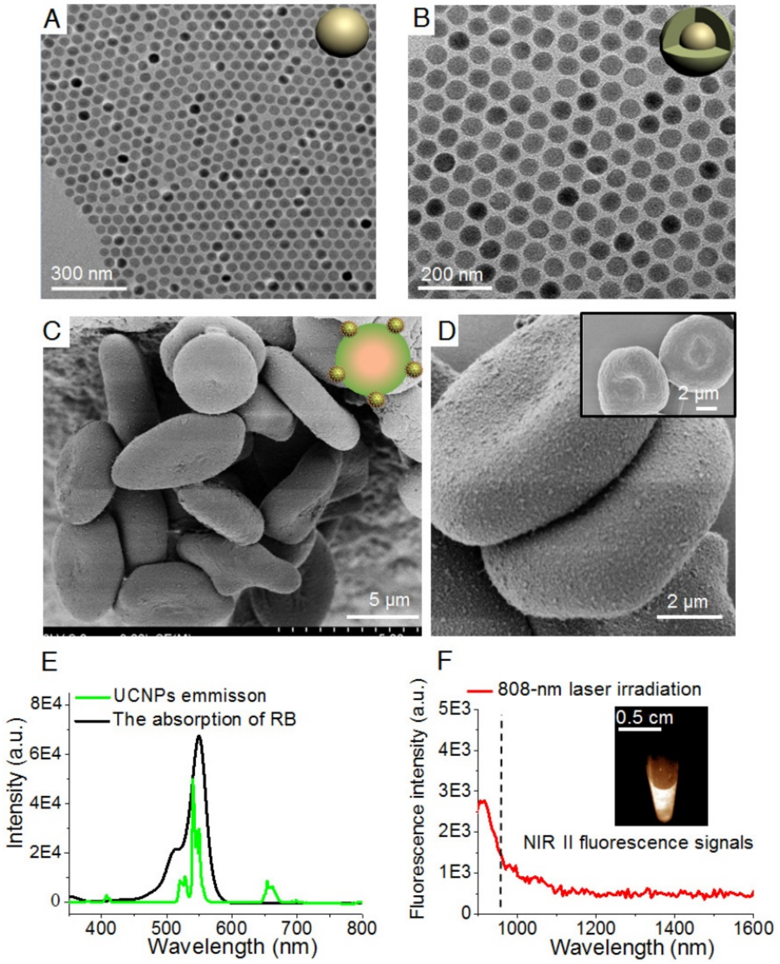

Figure 2. Characterization of RBCp. TEM images of core nanocrystals of NaGdF$_4$:Yb,Er **(A)** and NaGdF$_4$:Yb,Er@NaGdF$_4$ with the core-shell nanostructure **(B)**. **(C)** SEM images of RBC-based multimodal probes and **(D)** the enlarged image with higher magnification of two RBC-based multimodal probes attached with UCNPs; insert: RBCs without UCNPs modification. **(E)** The emission spectrum of UCNPs under a 980-nm laser irradiation and the absorption spectrum of RB. **(F)** The emission spectrum of aqueous ICG solution under an 808-nm laser irradiation; insert: NIR II fluorescence image of ICG observed by InGaAs camera (100 ms exposure time, 1000 nm long-pass filter).

intratumor blood O_2 saturation from 13% to 30% after a 10-min laser irradiation (**Figure 3F** and **Figure S13**). Compared with the bare RBCp without laser irradiation, for which no obvious oxygenated hemoglobin signal was observed, the aforementioned results indicate that *in vivo* O_2 and ICG can only be released in response to an 808-nm laser irradiation.

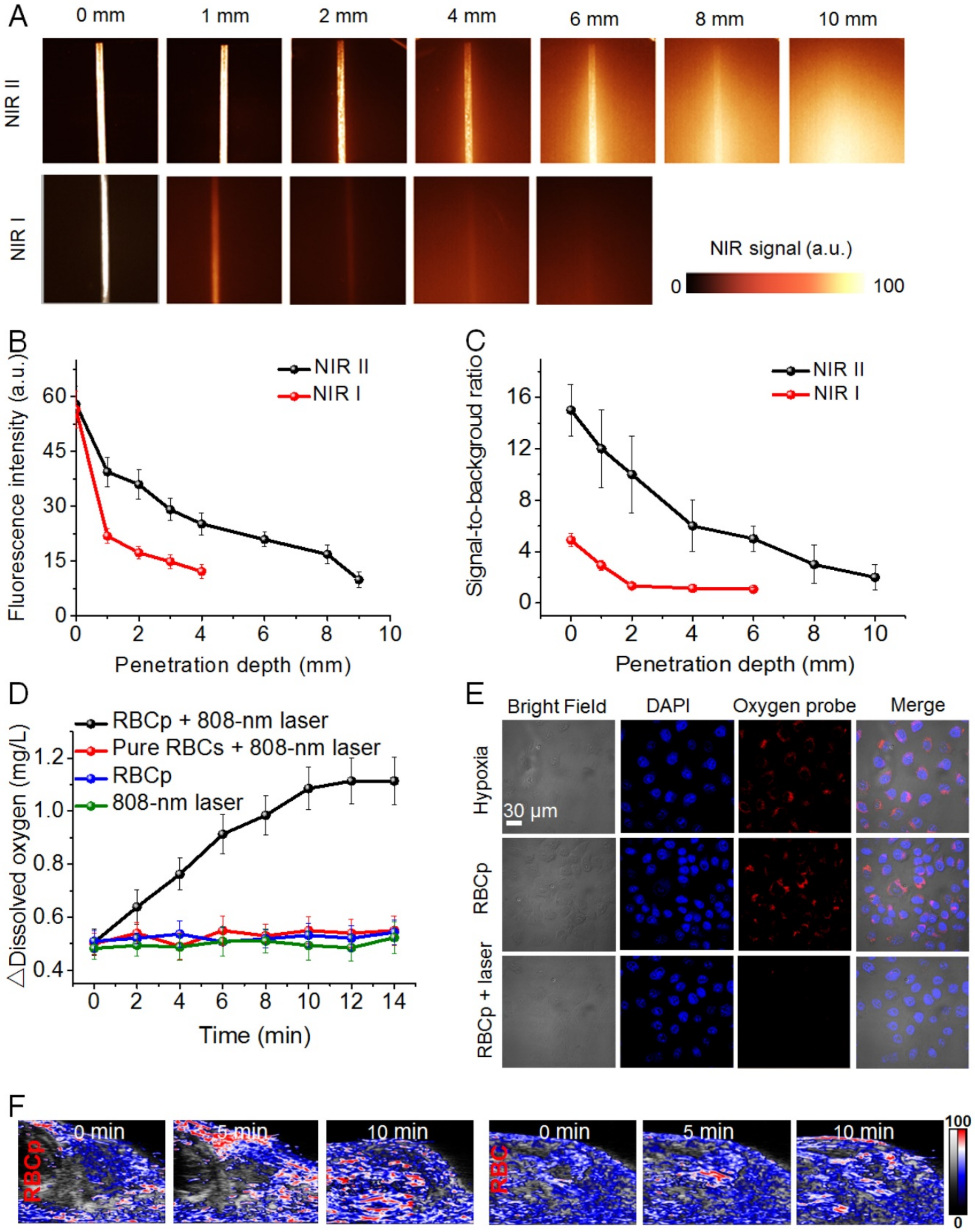

Figure 3. **NIR II fluorescence imaging and laser activated O_2 release of RBCp. (A)** NIR I and NIR II fluorescent images of ICG show complete attenuation of NIR I light within 4 mm, while the NIR II light is able to be detected through 8 mm of phantom tissues. The corresponding fluorescence intensities **(B)** and signal-to-background ratios **(C)** of both NIR I and NIR II fluorescence as a function of tissue phantom depth. **(D)** *In vitro* O_2 generation of RBCp with and without an 808-nm laser irradiation; pure RBCs with an 808-nm laser irradiation were set as a control group. **(E)** O_2 release of RBCp in hypoxic HepG2 cells with and without exposure to an 808-nm laser for 10 min. All of the images were obtained by a confocal laser scanning microscope. **(F)** 2D photoacoustic images of epidermal liver tumors with RBCp and RBC injection to detect the blood O_2 saturation in the vasculature, by an 808-nm laser irradiation for 0, 5 and 10 min. Representative images are from n = 4. Error bars indicate SD (n = 4).

In addition, after intracellular O_2 release under an 808-nm laser exposure, the ROS generation of RBCp upon a 980-nm laser irradiation was tested. Here, the ROS generation was studied by a hydrophilic ROS indicator, 9,10-anthracenediyl-bis(methylene)dimalonic acid (ABDA), for which the absorption intensity at 400 nm would decrease after reacting with the generated $^1O_2$. As shown in **Figure S14**, the absorption intensity of ABDA in the group of RBCp with a dual 808 nm and 980 nm laser irradiation was significantly decreased compared with the pure ABDA without RBCp but with the same laser irradiation, or with RBCp irradiated only by a 980-nm laser, demonstrating a massive $^1O_2$ generation due to O_2 release from RBCp under an 808-nm laser exposure. Based on the efficient ROS generation in aqueous solution, the generation of ROS in hypoxic HepG2 cells was assessed after incubating with RBCp followed by alternating irradiation by 808 nm and 980 nm lasers. The ROS generation efficiency of RBCp in HepG2 cells under hypoxic conditions (i.e., incubator set at 5% CO_2, 93% N_2 and 2% O_2) was estimated by a fluorescent marker, dichlorofluorescein diacetate. Upon extending the 808-nm laser exposure time for intracellular O_2 release (from 1 to 10 min), stronger signals of the $^1O_2$ marker were also significantly increased under a simultaneous 980-nm irradiation (**Figure S15**). However, no obvious $^1O_2$ generation in the control group was observed (without 808-nm laser irradiation), resulting from a lack of O_2 release in the hypoxic cytoplasm (**Figure S15**), which further confirmed that the RBCp can be applied for hypoxic tumor-specific PDT. Furthermore, the loaded ICG in RBCp alone could not generate enough $^1O_2$ for efficient cancer cell killing only with 808 nm laser irradiation (**Figures S16-S17**). The aforementioned results demonstrated that the RB on RBCp could be triggered for ROS generation within the hypoxic cytoplasm on account of the site-specific O_2 release from RBCs, thereby representing an ideal PDT platform for hypoxic tumor inhibition. The most significant cytotoxicity on hypoxic HepG2 cells was obtained with RBCp incubation followed by alternately irradiating with 808 nm and 980 nm lasers (50% cell viability in hypoxic conditions and 19% cell viability in normoxic conditions, **Figure S18**), further suggesting that excellent PDT efficiency could be realized due to the massive intracellular O_2 release.

NIR II fluorescence bioimaging-guided liver tumor surgery

Although no FDA-approved contrast agents with a peak emission in the NIR II region yet exist, observing the nonpeak fluorescence of clinically accessible NIR dyes in the NIR II region, such as ICG, has been proven to possess the potential for rapid translation of NIR II fluorescence bioimaging to clinical applications [43]. Here, the NIR II fluorescence imaging system for tumor surgical guidance with a ~30 cm working distance and 40 mW/cm^2 fluence rate was used for an *in vivo* NIR II fluorescence investigation (**Figure S19**) [52,53]. Unfortunately, we found that after the tail vein injection of ICG, the reagent strongly accumulated within the liver and then gradually entered into the intestinal system. However, no NIR II fluorescence signals were observed in the tumor, suggesting that ICG might not be directly applicable for clinical image-guided tumor surgery (**Figure S20**). Based on the aforementioned results, in order to further study whether RBCp could alter the tumor retention kinetics of NIR II nanoprobes in a favorable manner, *in vivo* experimentation was then carried out in subcutaneous human liver adenocarcinoma-bearing mice under an 808-nm laser irradiation. As expected, the circulation time of RBCp was similar to that of the unmodified RBCs, demonstrating the advantages of the RBC-based drug delivery system (**Figure S21**). After a tail vein intravenous injection of RBCp (10 mg/kg), the NIR II fluorescence signals in liver could be clearly observed at 2 h PI, then showed a minimum signal in the liver at approximately at 10 h PI (**Figure 4A**). Furthermore, the NIR II fluorescent signals can be observed within the tumor at 4 h PI; they attain maximum values at 10 h PI and remain essentially unchanged from this time until 13 h PI. Then, the fluorescence of the tumor site gradually faded from 14 h PI onward, and almost no signal was observed after 30 h PI (**Figure 4A**). The process from the beginning of accumulation to the end of complete metabolism of our RBCp at tumor sites could be monitored by NIR II fluorescence bioimaging. The UCNPs were still linked to the membrane of RBCs even after delivery into tumors (**Figure S22**); therefore, the quantitative analysis of RBCp biodistribution in liver and tumors could be further analyzed by inductively coupled plasma mass spectrometry (ICP-MS) according to Gd^{3+} concentrations from UCNPs. The results showed that the liver accumulation of RBCp was enriched intensely at 2 h PI (56.2% ID/g) and then drastically decreased according to the liver accumulation half-life of ~10 h. After 13 h PI, there was only minimal residual RBCp within the liver (13.1% ID/g), demonstrating the rapid clearance ability of the liver for our RBCp. Meanwhile, the tumor accumulation was gradually increased from 2 h PI, and the maximum tumor retention of our probes was observed at 10 h PI (11.5% ID/g), then maintained from 10 h PI to 13 h PI. These findings are in agreement with the results of NIR II fluorescence bioimaging, revealing a stable tumor retention period from 10 h to 13 h PI (**Figure 4B**). Subsequently, tumor retention continuously decreased to below 4.9% ID/g after 24 h PI, demonstrating that the RBCp are typically cleared from the tumor (**Figure 4B**). The aforementioned liver and tumor accumulation results demonstrated that the RBCp can be rapidly cleared with low amounts in the liver while displaying a stable and efficient tumor retention from 10 to 13 h PI. These results inspire us to investigate the tumor-to-liver ratio (T/L) after the intravenous injection of RBCp. There was a nearly 4 h stable tumor retention time during which T/L remained at a constant value ~11.5 from 10 h to 13 h PI (**Figure 4C**). To realize precise image-guided tumor resection, it is crucial to ensure that the full outlines of tumors with various sizes can be visualized during surgery. Based on this expectation, the stable T/L from 10 to 13 h PI allows for an accurate image-guided tumor-removal surgery within this “surgical window” (**Figure 4C**). Furthermore, the T/L ratios of RBCp are similar to those of RBCp without UCNPs yet significantly higher than those of RBCp without RGD, suggesting that the UCNPs anchor has no effect on either the targeting efficiency or the excellent tumor accumulation ability conferred by the RGD modification (**Figure 4D** and **Figures S23-S24**). Based on the aforementioned results, tumors were resected in this surgical window (**Video S1**) and then estimated by the pathological analysis of hematoxylin and eosin (H&E) staining. The remarkable boundary line between tumor and normal tissues revealed the superior tumor margin delineation ability of RBCp in the surgical window (**Figure 4E**). Meanwhile, the resected tumor at 14 h PI exhibits no borderline between the tumor and normal tissues in comparison to those operated during 10 to 13 h PI (**Figure 4E**), further suggesting that the tumors can only be detected and completely resected in this surgical time window. The orthotopic model also demonstrated the same body clearance kinetics as the subcutaneous model [15], suggesting that our RBCp can be further applied for actual applications.

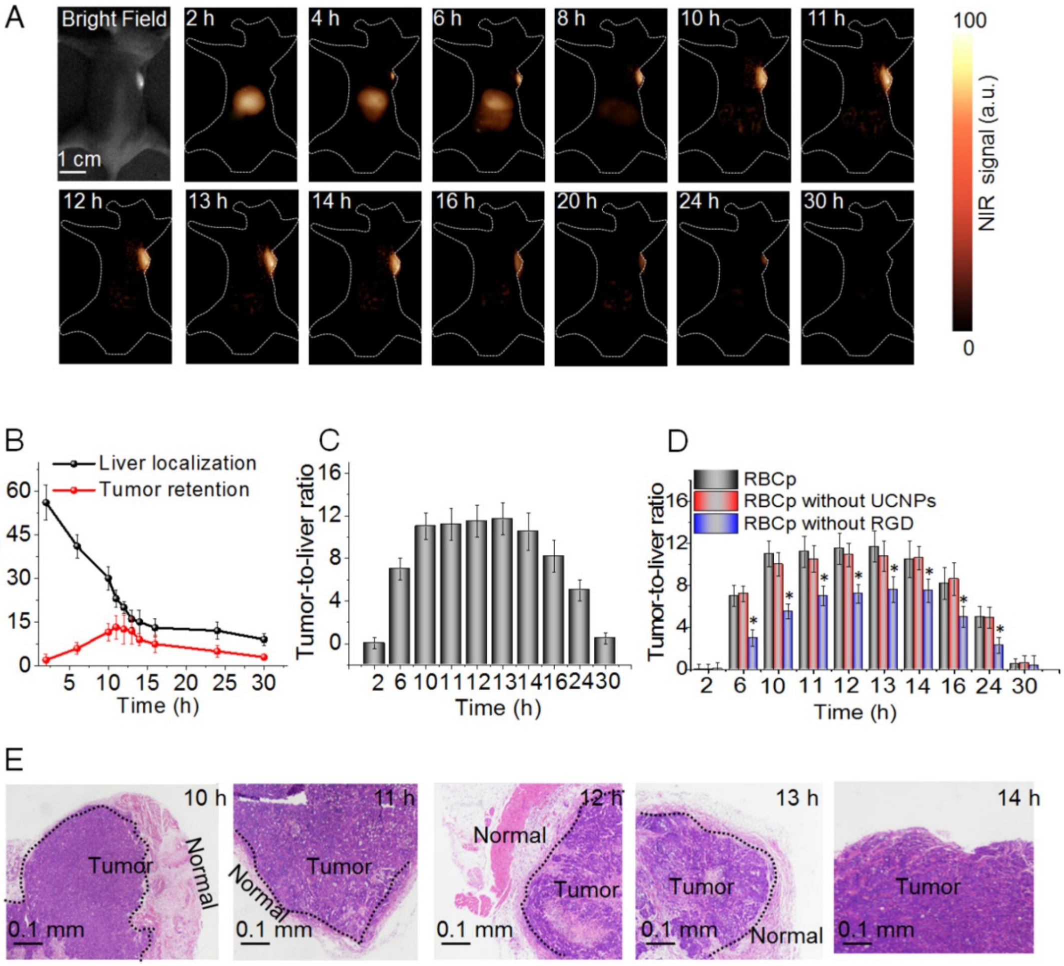

Figure 4. Optimal NIR II fluorescence imaging time window for surgery. (A) NIR II fluorescence bioimaging (100 ms exposure time, 1000 nm long-pass filter) of a subcutaneous tumor-bearing nude mouse with a single tail vein RBCp injection under an 808-nm excitation (0.2 W/cm²). **(B)** Liver distribution and tumor targeting efficiency of RBCp. **(C)** Tumor-to-liver ratio after an intravenous injection of RBCp. **(D)** Tumor-to-liver ratio of RBCp, RBCp without UCNPs modification and RBCp without RGD motif targeting. **(E)** H & E staining results of the tumors removed from 10 - 14 h post injection (PI) under the guidance of NIR II fluorescence bioimaging. Representative images are from n = 4. Error bars indicate SD (n = 4).

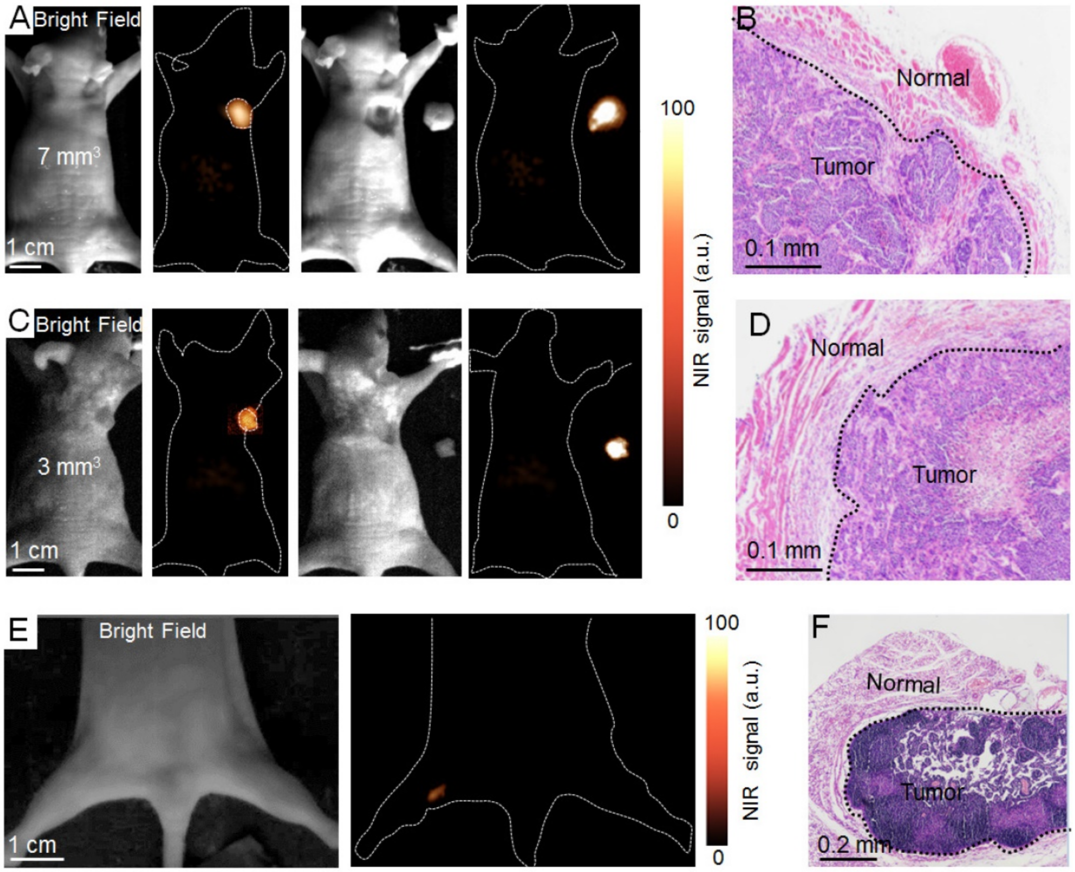

Figure 5. NIR II fluorescence imaging guided tumor surgery. NIR II fluorescence bioimaging results (12 h PI) of epidermal tumors with sizes of 7 mm^3 **(A)** and 3 mm^3 **(C)** and NIR II fluorescence bioimaging results after the surgical resection of tumors. **(B, D)** H&E staining results of the tumor and normal tissue boundary in A and C, respectively. **(E)** The NIR II bioimaging results (12 h PI) of popliteal lymph node metastasis. **(F)** H & E staining results of popliteal lymph node metastasis. The metastasis was resected under the navigation of NIR II fluorescence bioimaging.

The full outline of tumors with ~7 mm^3 and ~3 mm^3 can be visualized by NIR II bioimaging in this superior time window (**Figure 5A, C**). H&E staining was investigated after all tumors were resected under the guidance of NIR II fluorescence bioimaging, demonstrating the precise identification of tumor margins with different volumes (**Figure 5B, D**). To investigate whether RBCp can be applied to other metastasis models, we finally investigated the potential application of the RBCp for intraoperative imaging in a liver popliteal lymph node metastases model (**Figures S25-S26**). Significantly, the metastatic lesion can be successfully identified by NIR II fluorescence bioimaging in the optimal surgical window (**Figure 5E**). H&E staining results displayed that the metastasis was completely removed, further confirming that the long tumor retention period (~4 h) of RBCp was sufficient for correctly identifying lymph node metastases (**Figure 5F**).

NIR II fluorescence bioimaging-guided PDT after O$_2$ release for metastases

Encouraged by the advantages of the O$_2$ delivery and NIR II fluorescence bioimaging properties of RBCp, the PDT efficiency of RBCp was eventually evaluated. The $^1O_2$ can be generated from RB for efficiently killing tumor cells with 540 nm upconversion fluorescence from UCNPs under a 980-nm laser excitation [54]. Additionally, NIR II fluorescence imaging can be applied to PDT guidance for the treatment of popliteal lymph node metastasis-bearing mice after a tail vein injection of RBCp. As shown in **Figure 6A-B**, a significantly enhanced therapeutic efficiency was obtained in RBCp-treated mice with an 808-nm laser irradiation for O$_2$ release and a subsequent 980-nm laser exposure for $^1O_2$ generation. The tumor inhibition results of this treatment further proved the tumor oxygenation property of RBCp, resulting in the highest anti-tumor efficacy by remarkably inhibiting tumor volumes (**Figure 6A-B, D** and **Figures S27-S28**). The *in vivo* toxicity of RBCp was further analyzed by conventional H&E staining (**Figure S29**). Compared with the control groups, almost no obvious tissue damage or any other side effects were observed in spleen, lung, liver, heart, and kidney, indicating that no obvious side effects occur in the body after RBCp-facilitated PDT. Moreover, there was no unexpected skin damage caused by NIR laser irradiation during *in vivo* experiments (**Figure S30**). Simultaneously, no weight fluctuations were observed and no interferon-α (IFN-α) level increase in blood samples was monitored, further indicating good biocompatibility and the ability of avoiding immune response of RBCp (**Figure 6C** and **Figure S31**).

Conclusion

In conclusion, we have designed RBC-based multimodal theranostic probes for simultaneous bioimaging and PDT enhancement. RBCp experienced efficient tumor targeting and long tumor retention after an intravenous injection. The NIR II fluorescence of ICG is first reported for bioimaging-guided tumor surgery. A stable tumor retention period of RBCp was experienced for 4 h, and the superior T/L can be used for precise tumor resection under an 808-nm laser irradiation. Notably, in this retention period, RBCp can facilitate lymph popliteal metastasis surgical delineation. Meanwhile, RBCp can provide a laser-responsive O_2 releasing effect to enhance PDT efficiency under the guidance of NIR II fluorescence. These excellent performances obviously lead to remarkably enhanced synergistic therapeutic effects of tumor surgery and metastasis inhibition. We envision that the above-designed RBCp could shed light on precise identification of solid tumor margins in order to guide and optimize therapeutic procedures.

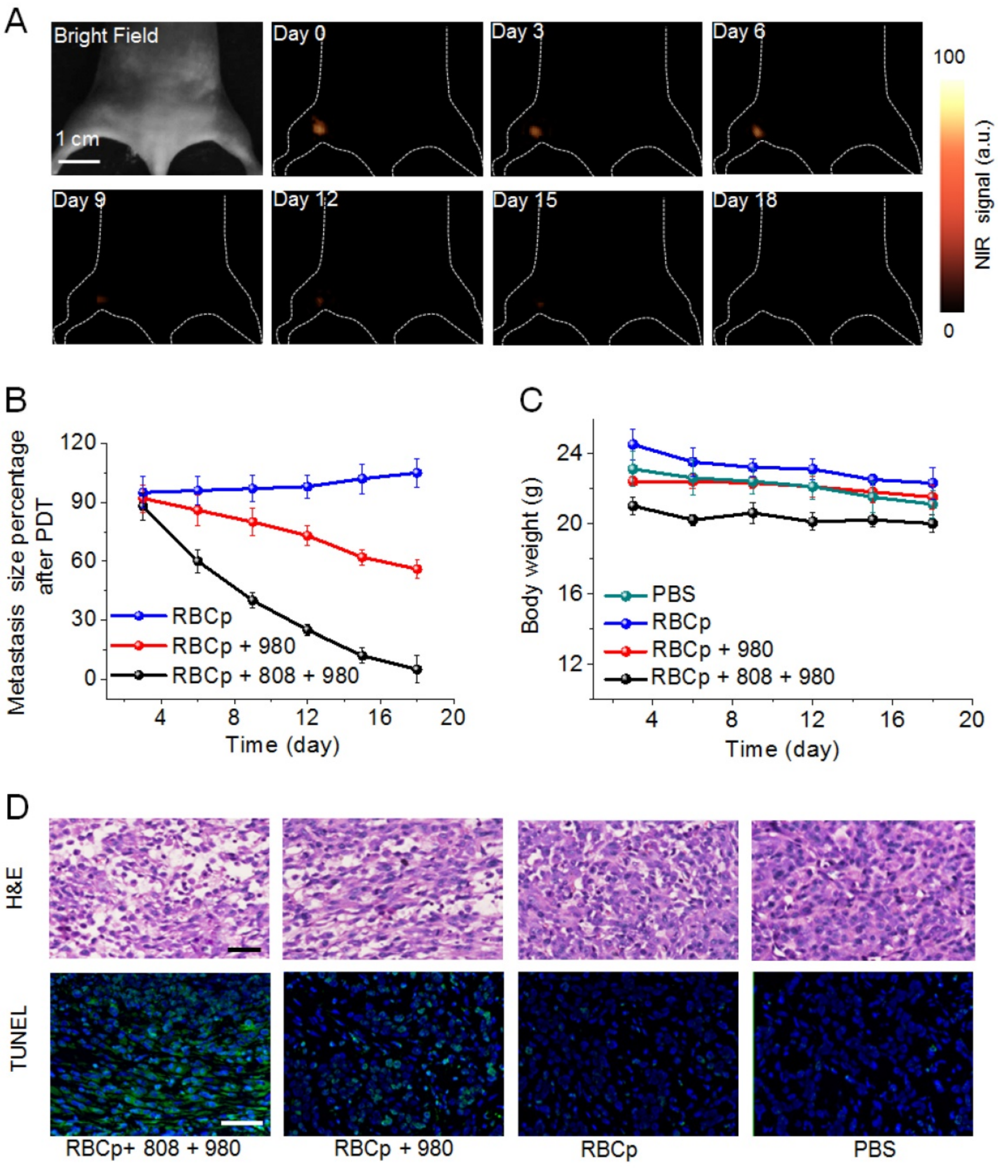

Figure 6. **NIR II fluorescence imaging guided PDT of RBCp. (A)** NIR II fluorescence bioimaging-guided PDT of popliteal lymph node metastasis-bearing mice by RBCp injection and alternate irradiation with 808-nm and 980-nm laser. **(B)** Popliteal lymph node metastasis growth profiles after a quantitative NIR II fluorescence analysis of all images in A. **(C)** Weight change curves of popliteal lymph node metastasis-bearing mice after different treatments for 18 days. **(D)** H&E and TUNEL staining images of the tumors after 3 days of indicated treatments. Scale bars represent 100 μm. Representative images are from n = 4. Error bars indicate SD (n = 4).

Methods

Preparation of RBC-based multimodal theranostic probes

Coating of compact DSPE-PEG$_{2000}$-NH$_2$ onto the surface of UCNPs. Five mL of 0.1 mmol oleic acid-modified UCNPs in chloroform was mixed with 1 mL of 25 mg DSPE-PEG$_{2000}$-NH$_2$ chloroform solution in a round-bottom flask. Then, the chloroform was gradually evaporated under stirring for 2 days at room temperature. Finally, the above-prepared sample was hydrated with 5 mL of DI water, and then the obtained amino phospholipid-modified UCNPs (hydrophilic) were dispersed after vigorous sonication. Excess amino phospholipids were further purified from the hydrophilic UCNPs more than 3 times by centrifugation at 17,500 rpm for 30 min. To remove large aggregates, the washed sample was finally filtered by 0.22-μm filters.

RB, avidin and RGD-functionalized UCNPs were prepared as follows. The hexanoic acid ester-modified RB was first acquired by reacting RB with hexanoic acid, and then adopted for modification. To covalently bind RB, avidin and RGD onto UCNPs, dimethyl formamide (5 mL) solution containing 10 mg hexanoic acid ester-modified rose bengal, 4 mg avidin and 4 mg RGD, 15 mg EDC, and 15 mg of NHS were mixed together and incubated for 2 h at room temperature. Then, 0.1 mmol of DSPE-PEG$_{2000}$-NH$_2$-modified UCNPs was slowly added into the aforementioned mixture and vigorously stirred for 2 days. UCNPs@RB@RGD@avidin complexes were then washed by water to get rid of excess RB, avidin, and RGD. Compared with the singlet oxygen quantum yield of free RB ($\Phi_\triangle = 0.14$), the UCNPs@RB@RGD@avidin complexes have a comparable singlet oxygen quantum yield ($\Phi_\triangle = 0.12$), which could guarantee a high ROS generation efficiency for our RBCp.

Surface modification of RBC membranes was conducted as follows. RBC surface functionalization is obtained by following a previously reported method [47]. To prepare biotin-modified membranes of RBCs, 400 μL concentrated RBCs were redispersed in PBS (4 mL, 1 X, pH 7.4). Then, 0.5 mg DSPE–PEG$_{2000}$–biotin was added and incubated for half an hour at 37 °C with constant stirring. Meanwhile, 0.1 mg DSPE-PEG$_{2000}$-RGD was also anchored onto RBC membranes for the *in vivo* bioimaging investigation, following the same strategy. These biotin/RGD-modified RBCs were washed twice with PBS at 400 *x*g for 5 min and finally redispersed in PBS (1 X, pH 7.4).

ICG loading onto RBCs was achieved as follows. One hundred μL of the aforementioned RBCs-biotin was added into a dialysis bag (3.5 kD molecular weight), mixing together with 1 mL of 30 mg mL^{-1} ICG-BSA. A 50-mL dialysis medium was prepared as follows: 5×10^{-3} M NaHCO$_3$, 5×10^{-3} M NaH$_2$PO$_4$, 10×10^{-3} M glucose, 2×10^{-3} M MgCl$_2$, 1×10^{-3} M ATP, and 1.5×10^{-3} M reduced GSH. This dialysis process was allowed to occur over 20 min at 4 °C. RBCs resealing was achieved by dialyzing RBCs in the medium containing PIGPA-NaCl (10%) for half an hour at 37 °C. The resealed RBCs were further washed with ice cold PBS (1 X, pH 7.4) and centrifuged 4 times at 400 *x*g to remove excess BSA-ICG. Meanwhile, the RBC-ICG-RGD-biotin multimode probes were also obtained by the same procedure as that of the RBC-RGD-biotin molecules and were used instead of RBC-biotin.

Preparation of RBC based multimodal probes. RBC@ICG@biotin and UCNPs@RB@RGD@avidin were mixed together for 1 h at 4 °C under stirring, and then the sample was washed twice with PBS. Finally, RBCp or RBCp without RGD modification were stored at 4 °C for further usage.

Scanning Electron Microscopy (SEM). The RBCp was first fixed with 2.5% glutaraldehyde by dropwise adding over 40 min in a 4°C refrigerator. Then, the RBCp was washed twice with DI water. Afterwards, the above-washed RBCp was dehydrated by ethanol with concentrations of 50, 60, 70, 80, 90, and 100% for 15 min. The RBCp suspensions were finally dropped onto the surface of glass coverslips; after drying at room temperature, they were coated onto Au nanoparticles before an observation under the scanning electron microscope.

NIR II fluorescence bioimaging-guided tumor surgery

The popliteal lymph node metastasis model was obtained as follows. All animal experiments were approved by the Animal Ethics Committee of the Chinese Academy of Sciences. The left hind paws of five-week-old mice were inoculated with HepG2 cells (5×10^8 cells/mouse). At 21 days after the intradermal injection, these tumor cells spontaneously formed lymph node metastases in the popliteal lymph nodes.

NIR II fluorescence bioimaging was conducted as follows. When the tumor volume reached 0.4 - 0.7 cm^3 (10 - 11 days after tumor tissue implantation), the subcutaneous tumor-bearing mice were used for bioimaging investigation. Then, the mice with epidermal tumors were intravenously injected with RBCp, RBCp without UCNPs and RBCp without RGD in physiological saline (10 mg/kg). *In vivo* bioimaging experiments were performed by an NIR InGaAs CCD camera equipped with an adjustable 808-nm laser (0.2 W/cm^2, 30 cm working distance) as the excitation source. The optical whole body bioimages of tumor-bearing mice were recorded by the NIRvana

InGaAs CCD camera at 0 - 30 h PI. For *ex vivo* tumor retention and liver localization analysis, mice were sacrificed at different hours PI. Livers and tumors were then collected, measured and weighed. RBCp biodistribution was determined by an ICP-MS analysis.

The orthotopic tumors can be successfully detected under NIR II fluorescence bioimaging within the optimal surgical window (10 - 13 h PI). Tumors were resected 10 h, 11 h, 12 h and 13 h PI under the guidance of NIR II fluorescence bioimaging. Meanwhile, tumors were also removed after the optimal surgical time window (14 h PI). All tumors were further verified by H&E staining analysis. The eye-invisible ultra-small popliteal lymph node metastases were resected under the NIR InGaAs CCD camera at 12 h PI. All collected tumor tissues were finally verified by H&E staining.

NIR II bioimaging-guided PDT of popliteal lymph node metastasis

The popliteal lymph node metastasis-bearing mice were divided into 4 groups including 4 mice of each: PBS, RBCp, RBCp + 980-nm laser irradiation and RBCp + 808 nm laser irradiation + 980 nm laser irradiation (808-nm laser = 0.5 W/cm^2, time = 10 min; 980-nm laser = 1.5 W/cm^2, time = 15 min; 5-min laser exposure with 5-min intervals). After 18 days of different treatments, an 808-nm NIR laser irradiation was carried out 12 h after injection. Body weight and DCL (downconversion luminescence) images were obtained the day after the 808-nm laser irradiation. The tumors were removed 3 days after the different treatments and then fixed by 10% formaldehyde. All tumors were analyzed by H&E and TUNEL staining for tumor cell apoptosis analysis. All of the resected organs, including liver, spleen, lung, heart and kidney, were further analyzed by H&E staining after 18 days of treatment.

Abbreviations

ABDA: 9,10-anthracenediyl-bis(methylene)dimalonic acid; BSA: bovine serum albumin; CCD: charge-coupled device; CLSM: confocal laser scanning microscope; DCL: downconversion luminescence; EDC: 1-ethyl-3-(3′-dimethylaminopropyl)carbodiimide; HbO_2: oxygenated hemoglobin; H&E: hematoxylin and eosin; ICG: indocyanine green; ICP-MS: inductively coupled plasma mass spectrometry; IFN-α: interferon-α; MB: methylene blue; NHS: N-hydroxysuccinimide; NIR I: first near-infrared window; NIR II: second near-infrared window; PA: photoacoustic; RB: rose bengal; RBCs: red blood cells; RGD: Arg-Gly-Asp; ROS: reactive oxygen species; T/L: tumor-to-liver ratio; TUNEL: terminal deoxynucleotidyl transferase-mediated nick end labeling; UCNPs: upconversion nanoparticles.

Acknowledgements

This work was supported by the National Natural Science Foundation of China (Grant No. 61727823, Grant No. 81671813, Grant No. 61575044, Grant No. 81871483 and Grant No. U1505221) and the Joint Funds for the Innovation of Science and Technology, Fujian province (Grant No. 2016Y9062).

Supplementary Material

Supplementary figures and tables.
http://www.thno.org/v09p0369s1.pdf

Competing Interests

The authors have declared that no competing interest exists.

References

1. Rizzo M, Lyengar R, Gabram SG, Park J, Birdsong G, Chandler KL, et al. The effects of additional tumor cavity sampling at the time of breast-conserving surgery on final margin status volume of resection and pathologist workload. Ann Surg Oncol. 2010; 17: 228-234.
2. Andreou C, Neuschmelting V, Tschaharganeh DE, Huang CH, Oseledchyk A, Iacono P, et al. Imaging of liver tumors using surface-enhanced raman scattering nanoparticles. ACS Nano. 2016; 10: 5015-5026.
3. Vahrmeijer AL, Hutteman M, vander Vorst JR, vande Velde CJ, Frangioni JV. Image-guided cancer surgery using near-infrared fluorescence. Nat Rev Clin Oncol. 2013; 10: 507-518.
4. Antaris AL, Chen H, Cheng K, Sun Y, Hong G, Qu C, et al. A Small-molecule dye for NIR II imaging. Nat Mater. 2015; 15: 235-243.
5. Keereweer S, Van Driel PBAA, Snoeks TJA, Kerrebijn JDF, Baatenburg de Jong RJ, Vahrmeijer AL, et al. Optical image-guided cancer surgery: challenges and limitations. Clin Cancer Res. 2013; 19: 3745-3754.
6. Ghosh D, Bagley AF, Na YJ, Birrer MJ, Bhatia SN, Belcher AM. Deep noninvasive imaging and surgical guidance of submillimeter tumors using targeted m13-stabilized single-walled carbon nanotubes. Proc Natl Acad Sci USA. 2014; 111: 13948-13953.
7. van Dam GM, Themelis G, Crane LMA, Harlaar NJ, Pleijhuis RG, Kelder W, et al. Intraoperative tumor-specific fluorescence imaging in ovarian cancer by folate receptor-α targeting: first in-human results. Nat Med. 2010; 17: 1315-1319.
8. Brindle K. New Approaches for imaging tumors responeses to treatment. Nat Rev Cancer. 2008; 8: 94-107.
9. Urano Y, Sakabe M, Kosaka N, Ogawa M, Mitsunaga M, Asanuma D, et al. Rapid cancer detection by topically spraying a γ-glutamyltranspeptidase-activated fluorescent probe. Sci Transl Med. 2010; 3: 110-119.
10. Kamolz LP, Andel H, Auer T, Meissl G, Frey M. Evaluation of skin perfusion by use of indocyanine green video angiography: rational design and planning of trauma surgery. J Trauma. 2006; 61: 635-641.
11. Hong G, Lee JC, Robinson JT, Raaz U, Xie L, Huang NF, et al. Multifunctional in vivo vascular imaging using near-infrared II fluorescence. Nat Med. 2012; 18: 1841-1846.
12. Hong G, Zou Y, Antaris AL, Diao S, Wu D, Cheng K, et al. Ultrafast fluorescence imaging *in vivo* with conjugated polymer fluorophores in the second near-infrared window. Nat Commun. 2014; 5: 4206.
13. Diao S, Hong G, Robinson JT, Jiao L, Antaris AL, Wu JZ, et al. Chirality enriched (121) and (113) single-walled carbon nanotubes for biological imaging. J Am Chem Soc. 2012; 134: 16971-16974.
14. Wang R, Zhou L, Wang W, Li X, Zhang F. In vivo gastrointestinal drug-release monitoring through second near-infrared window fluorescent bioimaging with orally delivered microcarriers. Nat Commun. 2017; 8: 14072.
15. Wang PY, Fan Y, Lu LF, Liu L, Fan LL, Zhao MY, et al. NIR-II nanoprobes in-vivo assembly to improve image-guided surgery for metastatic ovarian cancer. Nat Commun. 2018; 9: 2898.
16. Naczynski DJ, Tan MC, Zevon M, Wall B, Kohl J, Kulesa A, et al. Rare-earth-doped biological composites as in vivo shortwave infrared reporters. Nat Commun. 2013; 4: 2199.
17. Jiang YY, Li JC, Zhen X, Xie C, Pu KY. Dual-peak absorbing semiconducting copolymer nanoparticles for first and second near-infrared window photothermal therapy: a comparative study. Adv Mater. 2018; 30: 1705980.

18. Jiang YY, Upputuri PK, Xie C, Lyu Y, Zhang LL, Xiong Q, et al. Broadband absorbing semiconducting polymer nanoparticles for photoacoustic imaging in second near-infrared window. Nano Lett. 2017; 17: 4964-4969.
19. Li JC, Zhen X, Lyu Y, Jiang YY, Huang JG, Pu KY. Cell membrane coated semiconducting polymer nanoparticles for enhanced multimodal cancer phototheranostics. ACS Nano. 2018; 12: 8520-8530.
20. Jiang YY, Pu KY. Multimodal biophotonics of semiconducting polymer nanoparticles. Acc Chem Res. 2018; 51: 1840-1849.
21. Castano A P, Mroz P, Hamblin MR. Photodynamic therapy and anti-tumour immunity. Nat Rev Cancer. 2006; 6: 535-545.
22. Braathen LR, Szeimies RM, Seguin NB, Bissonnette B, Foley P, Pariser D, et al. Guidelines on the use of photodynamic therapy for nonmelanoma skin cancer: an international consensus. J Am Acad Dermatol. 2007; 56: 125-43.
23. Wolf P, Rieger E, Kerl H. Topical Photodynamic Therapy with endogenous porphyrins after application of 5-aminolevulinic acid: an alternative treatment modality for solar keratoses superficial squamous cell carcinomas and basal cell carcinomas. J Am Acad Dermatol. 1993; 28: 17-21.
24. Celli JP, Spring BQ, Rizvi I, Evans CL, Samkoe KS, Verma S, et al. Imaging and photodynamic therapy: mechanisms monitoring and optimization. Chem Rev. 2010; 12: 2795-2838.
25. Zhu HJ, Fan Y, Miao QQ, Qi XY, Ding D, Chen P, et al. Regulating near-infrared photodynamic properties of semiconducting polymer nanotheranostics for optimized cancer therapy. ACS Nano, 2017; 11: 8998-9009.
26. Li JC, Xie C, Huang JG, Jiang YY, Miao QQ, Pu KY. Semiconducting polymer nanoenzymes with photothermic activity for enhanced cancer therapy. Angew Chem Int Ed, 2018; 57: 3995-3998.
27. Maas ML, Carter SL, Wileyto EP, Miller J, Yuan M, Yu G, et al. Tumor vascular microenvironment determines responsiveness to photodynamic therapy. Cancer Res. 2012; 72: 2079-2088.
28. Henderson BW, Fingar VH. Relationship of tumor hypoxia and response to photodynamic treatment in an experimental mouse tumor. Cancer Res. 1987; 47: 3110-3114.
29. Jin CS, Lovell JF, Chen J, Zheng G. Hypoxic tumors with dose-equivalent photothermal but not photodynamic therapy using a nanostructured porphyrin assembly. ACS Nano. 2013; 7: 2541-2550.
30. Wang W, Moriyama LT, Bagnato VS. Photodynamic therapy induced vascular damage: an overview of experimental PDT laser. Phys Lett. 2013; 10: 023001-0023008.
31. Henderson BW, Dougherty TJ. How does photodynamic therapy work? Photochem Photobiol. 1992; 55: 145-157.
32. Gomer CJ, Razum NJ. Acute skin response in albino mice following porphyrin photosensitization under oxic and anoxic conditions. Photochem Photobiol. 1984; 40: 435-439.
33. Tang W, Zhen Z, Wang M, Wang H, Chuang Y, Zhang W, et al. Red blood cell-facilitated photodynamic therapy for cancer treatment. Adv Funct Mater. 2016; 26:1757-1768.
34. Wilson WR, Hay MP. Targeting hypoxia in cancer therapy. Nat Rev. 2011; 11: 393-410.
35. Brown JM, Wilson WR. Exploiting tumour hypoxia in cancer treatment. Nat Rev. 2014; 4: 437-447.
36. Chen Y, Chen H, Jiang C, Qiu X, Wang K, Huan W, et al. Perfluorocarbon nanoparticles enhance reactive oxygen levels and tumour growth inhibition in photodynamic therapy. Nat Commun. 2015; 6: 8785.
37. Song G, Liang C, Yi X, Zhao Q, Cheng L, Yang K,et al. Perfluorocarbon-loaded hollow Bi_2Se_3 nanoparticles for timely supply of oxygen under near-infrared light to enhance the radiotherapy of cancer. Adv Mater. 2016; 28: 2716-2723.
38. Gong H, Chao Y, Xiang J, Han X, Song G, Feng L, et al. Hyaluronidase to enhance nanoparticle-based photodynamictumor therapy. Nano Lett. 2016; 16: 2512-2521.
39. Fan W, Bu W, Shen B, He Q, Cui Z, Liu Y, et al. Intelligent MnO_2 nanosheets anchored with upconversion nanoprobes for concurrent pH-/H_2O_2-responsive ucl imaging and oxygen-elevated synergetic therapy. Adv Mater. 2015; 27: 4155-4161.
40. Chen H, Tian J, He W, Guo Z. H_2O_2-activatable and O_2-evolving nanoparticles for highly efficient and selective photodynamic therapy against hypoxic tumor cells. J Am Chem Soc. 2015; 137: 1539-1547.
41. Huang C, Chia W, Chuang M, Lin K, Hsiao C, Jin C, et al. An implantable depot that can generate oxygen in situ for overcoming hypoxia-induced resistance to anticancer drugs in chemotherapy. J Am Chem Soc. 2016; 138: 5222-5225
42. Doshi N, Zahr AS, Bhaskar S, Lahann J, Mitragotri S. Red blood cell-mimicking synthetic biomaterial particles. Proc Natl Acad Sci USA. 2009; 106: 21495-21499.
43. Carr JA, Franke D, Caram JR, Perkinson CF, Saif M, Askoxylakis V, et al. Shortwave infrared fluorescence imaging with the clinically approved near-infrared dye indocyanine green. Proc Natl Acad Sci USA. 2018; 115: 4465-4470.
44. Starosolski Z, Bhavane R, Ghaghada KB, Vasudevan SA, Kaay A, Annapragada A. Indocyanine green fluorescence in second near-infrared (NIR-II) window. Plos one. 2017; 12: e0187563.
45. Beutler E, Dale G, Guinto D, Kuhl W. Enzyme Replacement therapy in gaucher's disease: preliminary clinical trial of a new enzyme preparation. Proc Natl Acad Sci USA. 1977; 74: 4620-4623.
46. Kinosita K, Tsong TY. Survival of sucrose-loaded erythrocytes in the circulation. Nature. 1978; 272: 258-260.
47. Biagiotti S, Rossi L, Bianchi M, Giacomini E, Pierige F, Serafini G, et al. Immunophilin-loaded erythrocytes as a new delivery strategy for immunosuppressive drugs. J Controlled Release. 2011; 154: 306-313.
48. Liu K, Liu X, Zeng Q, Zhang Y, Tu L, Liu T, et al. Covalently assembled NIR nanoplatform for simultaneous fluorescence imaging and photodynamic therapy of cancer cells. ACS Nano. 2012; 6: 4054-4062.
49. Li X, Shen D, Yang J, Yao C, Che R, Zhang F, et al. Successive layer-by-layer strategy for multi-shell epitaxial growth: shell thickness and doping position dependence in upconverting optical properties. Chem Mater. 2013; 25: 106-112.
50. Yao C, Wang P, Zhou L, Wang R, Li X, Zhao DY, et al. Highly biocompatible zwitterionic phospholipids coated upconversion nanoparticles for efficient bioimaging. Anal Chem. 2014; 86: 9749-9757.
51. Chen Q, Wang C, Zhan ZX, He WW, Chen ZP, Li YY, et al. Near-infrared dye bound albumin with separated imaging and therapy wavelength channels for imaging-guided photothermal therapy. Biomaterials. 2014; 35: 8206-8214.
52. Schaafsma BE, Mieog JSM, Hutteman M, Van der vorst J, Kuppen PJK, Lowik CWGM, et al. The clinical use of indocyanine green as a near-infrared fluorescent contrast agent for image-guided oncologic surgery. J Surg Oncol. 2011; 104: 323-332.
53. Frangioni JV. In vivo near-infrared fluorescence imaging. Cur Opin Chem Biol. 2003; 7: 626-634
54. Wang P, Li X, Yao C, Wang W, Zhao M, El-Toni AM, et al. Orthogonal near-infrared upconversion co-regulated site-specific O2 delivery and photodynamic therapy for hypoxia tumor by using red blood cell microcarriers. Biomaterials. 2017; 125: 90-100.